JOURNAL OF SOLID STATE CHEMISTRY 62, 83–91 (1986)

Fluorescence and Energy-Transfer Characteristics of Rare Earth Ions in $BaYF_5$ Crystals

LIU XINGREN,* XU GANG, AND RICHARD C. POWELL

Department of Physics, Oklahoma State University, Stillwater, Oklahoma 74078

Received June 12, 1985; in revised form September 9, 1985

Fluorescence spectra, excitation spectra, and fluorescence lifetimes are reported for a series of $BaYF_5$ crystals doped with Eu^{2+}, Er^{3+}, or Ho^{3+}, or codoped with Eu^{2+} and either Er^{3+} or Ho^{3+} ions. These data were obtained as a function of concentration of active ions and temperature. The rate and efficiency of energy transfer between pairs of ions is obtained and the mechanism for energy transfer is found to be electric dipole–dipole interaction. In addition, multiphonon radiationless decay rates are determined for Er^{3+} in this host. © 1986 Academic Press, Inc.

Introduction

Doped fluoride crystals of the type $BaLnF_5$ and $BaLn_2F_8$ (Ln = La, · · · Lu, and Y) are an important class of materials for laser, phosphor, and upconversion applications (*1–5*). These host crystals can be simultaneously doped with divalent and trivalent rare earth ions. The former have strong, broad absorption bands ideal for optical pumping while the latter have sharp emission lines with much longer lifetimes ideal for generating stimulated emission. To make optimum use of these properties in designing materials for specific applications, it is important to characterize the process of energy transfer taking place between these two types of ions. This paper describes the fluorescence properties of $BaYF_5:Eu^{2+}$, $BaYF_5:Eu^{2+},Er^{3+}$, and $BaYF_5Eu^{2+},Ho^{3+}$ and presents the characteristics of energy transfer between Eu^{2+} and the trivalent rare earth ions in the latter two crystals.

The samples were prepared by solid state reaction of a stoichiometric mixture of fluorides in a pure nitrogen flow or N_2/H_2 mixture. The stoichiometric mixtures were loaded in graphite capsules and fired for about 20 hr at 1000°C. The $BaYF_5$ samples were checked by X-ray diffraction and found to be cubic with a unit cell dimension of 5.9 Å.

The samples were mounted in a cryogenic refrigerator capable of controlling the temperature between 10 and 300 K. For fluorescence spectra and lifetime measurements, excitation was provided by a nitrogen laser pulse 10 ns in duration and 1.0 Å in half width centered at 337.1 nm. The emission was focused onto the entrance slit of a 1-m Spex monochromator set for a resolution of 1 Å. The signal was detected by a cooled RCA C31034 photomultiplier tube and analyzed by an EGG/PAR boxcar inte-

* On leave from Changchun Institute of Physics, Chinese Academy of Science, Changchun, China.

0022-4596/86 $3.00

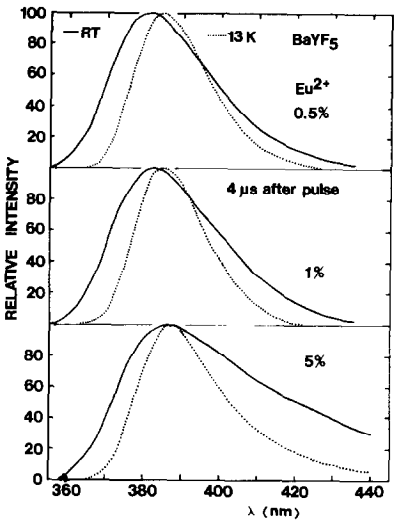

FIG. 1. Fluorescence spectra of Eu^{2+} in $BaYF_5$ at 4 μs after a nitrogen laser excitation pulse.

grator before being displayed on a strip-chart recorder. The boxcar window was either set to give time-resolved spectra or scanned to determine lifetimes. Excitation spectra were obtained with xenon lamp excitation.

Experimental Results

Spectra of $BaYF_5:Eu^{2+}$

The excitation spectra of the three Eu^{2+}-doped samples consist of two broad bands at approximately 260 and 332 nm which are similar to Eu^{2+} absorption bands reported in other host crystals. The nitrogen laser excitation efficiently pumps the low-energy absorption band. Figure 1 shows the fluorescence spectra of Eu^{2+} in $BaYF_5$ at 4 μs after the excitation pulse for three doping concentrations at both high and low temperatures. Each spectrum consists of a broad band in the near UV spectral region as is common for Eu^{2+} in other strong crystal field hosts. This is due to the allowed transition from the lowest level of the $4f^65d^1$ configuration to the ground state of the $4f^7$ configuration. The emission bands shown in Fig. 1 are broadened and shifted to lower energy as temperature is increased and as concentration of Eu^{2+} is increased.

The fluorescence decays for these samples were observed to be single exponentials with lifetimes less than a microsecond. These are listed in Table I. They were found to be independent of temperature and are typical magnitudes for parity- and spin-allowed transitions.

Spectra of $BaYF_5:Eu^{2+},Er^{3+}$

The room-temperature fluorescence spectrum of $BaYF_5:Eu^{2+},Er^{3+}$ after pulsed nitrogen laser excitation is shown in Fig. 2. The spectrum consists of two features: the first is the broad Eu^{2+} band similar to that

TABLE I

Eu^{2+}–Er^{3+} DECAY TIME AND ENERGY TRANSFER PARAMETERS (300 K)

Sample (mole %)		τ(μs)		t_r(μs)			
Eu	Er	Eu	Er	Er	η	$\omega(\mu s^{-1})$	R_0(Å)
0.5	0.0	0.71					
1.0	0.0	0.50					
5.0	0.0	0.21					
0.5	0.5	0.55			0.225	0.41	9.0
0.5	1.0	0.50			0.296	0.59	7.6
0.5	3.0	0.34	370	54	0.521	1.53	7.7
0.5	5.0	0.24			0.662	2.56	6.8

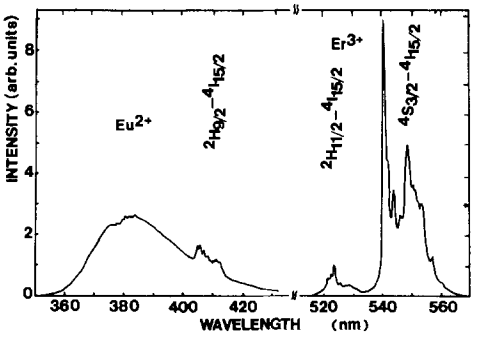

FIG. 2. Fluorescence spectrum of $BaYF_5$: Eu^{2+},Er^{3+} at room temperature.

seen in Fig. 1; the second is the series of sharp lines associated with the $4f$–$4f$ transitions of the Er^{3+} ions. The set of lines in the 540- to 560-nm spectral region corresponds to transitions between levels of the $^4S_{3/2}$–$^4I_{15/2}$ manifolds; those in the 522- to 535-nm region correspond to $^2H_{11/2}$–$^4I_{15/2}$ transitions; and the blue emission lines are associated with the $^2H_{9/2}$–$^4I_{15/2}$ transitions. The latter are weak but grow with increasing Er^{3+} concentration. The red emission of Er^{3+} associated with the $^4F_{9/2}$–$^4I_{15/2}$ transitions which is seen in other hosts is not observed in $BaYF_5$ at either high or low temperature under UV excitation. This may be due to reduced multiphonon relaxation rates in this host as discussed below. Infrared emission was not investigated.

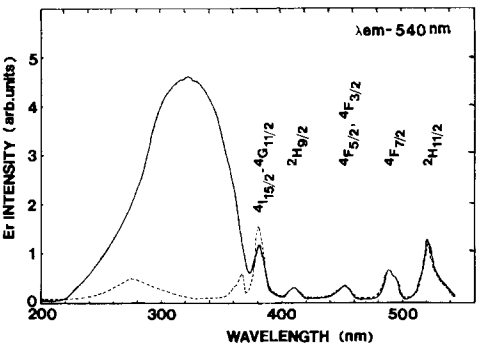

FIG. 3. Room-temperature excitation spectra of Er^{3+} emission of two samples at 540 nm with 0.5 mole% Er^{3+}. One sample contained no Eu^{2+} (broken line) and the other contained 0.5 mole% Eu^{2+}.

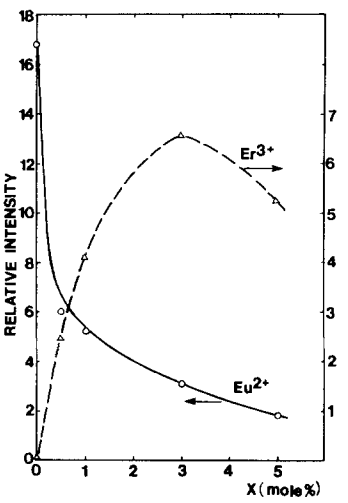

FIG. 4. Relative intensity of the Eu^{2+} emission at 380 nm and the Er^{3+} emission at 540 nm for samples of $BaYF_5$ containing 0.5 mole% Eu^{2+} as a function of X mole% Er^{3+} at room temperature.

Figure 3 compares the room-temperature excitation spectra of Er^{3+} in $BaYF_5$ samples with and without Eu^{2+}. Several sets of sharp lines belonging to Er^{3+} absorption transitions are observed in both spectra while the broad Eu^{2+} absorption band appears only in the Eu^{2+}-doped sample. These results show that efficient energy transfer occurs from Eu^{2+} to Er^{3+} ions in $BaYF_5$.

Figure 4 shows the fluorescence intensities of the Eu^{2+} emission at 381 nm and the Er^{3+} emission at 540 nm plotted as a function of the Er^{3+} concentration in $BaYF_5$ at room temperature. The Eu^{+} concentration is fixed at 0.5 mole% in these samples. The intensity of Er^{3+} emission increases while that of Eu^{2+} decreases with increasing Er^{3+} concentration up to about 3 mole%. This can be attributed to increased energy transfer efficiency as the average separation between Eu^{2+} and Er^{3+} ions decreases. At higher concentrations, the Er^{3+} emission intensity also decreases due to interactions between neighboring Er^{3+} ions.

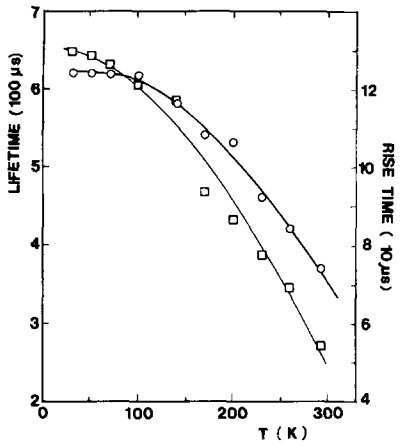

FIG. 5. Temperature dependence of the fluorescence lifetimes (circles) and rise times (squares) of Er^{3+} $^4S_{3/2}$ emission in $BaYF_5:Eu^{2+},Er^{3+}$ containing 0.5 mole% Eu^{2+} and 3.0 mole% Er^{3+}.

The fluorescence decay patterns of Er^{3+} after nitrogen laser excitation exhibit an initial rise and then an exponential decay. The temperature dependences of the rise and decay times are shown in Fig. 5 and the measured values are listed in Table I. Above about 100 K, the rise and decay times decrease similarly with increasing temperature. As temperature is lowered below 100 K the rise time continues to increase while the lifetime tends toward a constant value. The temperature dependence of the fluorescence lifetime is associated with the change in the rate of the multiphonon radiationless relaxation process from the $^4S_{3/2}$ level to the $^4I_{9/2}$ level. This is described by (*6–10*)

$$W_f = W_r + W_{nr} \tag{1}$$

with

$$W_{nr} = W(0)[e^{\hbar\omega/kT}/(e^{\hbar\omega/kT} - 1)]^p \tag{2}$$

where

$$W(0) = Ce^{-\alpha\Delta E}. \tag{3}$$

Here W_f, W_r, and W_{nr} are the fluorescence, radiative, and nonradiative decay rates, respectively. The latter is treated as the emission of p phonons of energy $\hbar\omega$ needed to cross an energy gap $\Delta E = p\hbar\omega$. $W(0)$ is the zero temperature rate for the multiphonon process and C and α are parameters associated with the specific host material. For the case of interest here, the energy gap is approximately 3030 cm^{-1}. The value for the maximum phonon energy in $BaYF_2$ has not been measured but should be of the order of 350 cm^{-1} as found for other fluoride crystals. This assumption leads to a $p = 9$ phonon process. Using these values in Eqs. (1) and (2), a good fit to the observed temperature dependence of the fluorescence lifetime can be obtained for values of $W_r = 1.44 \times 10^3$ sec^{-1} and $W_{nr} = 0.17 \times 10^3$ sec^{-1}. For other fluoride crystals the value of α has been determined to be close to 4×10^{-3} cm (*6*). Using this value in Eq. (3) gives a value for C of 3.1×10^7 sec^{-1}. This is consistent with the results of Johnson and Guggenheim on BaY_2F_8 crystals (*10*). The fact that W_r is an order of magnetude larger than W_{nr} at low temperatures is consistent with the fact that no fluorescence is observed from the $^4I_{9/2}$ level.

There can be two possible origins for the observed rise times in the fluorescence emission patterns. The first is the process of energy transfer from Eu^{2+} to Er^{3+} and the second is the process of radiationless relaxation from the higher energy levels of Er^{3+} down to the $^4S_{3/2}$ metastable state. The dominant contribution to the observed rise time is due to the process having the smallest transition rate. In both cases the expression for the rise time t_r is

$$t_r = (W_2 - W_f)^{-1} \ln(W_2/W_f) \tag{4}$$

where W_2 is either the energy transfer rate for the radiationless relaxation rate. The value for the energy transfer rate can be found from the quenching of the Eu^{2+} fluorescence lifetime as discussed below. If the value found in this way is substituted into Eq. (4) for W_2, the predicted value for t_r is

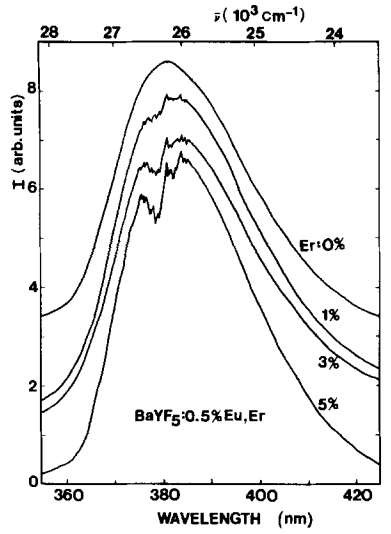

FIG. 6. Fluorescence spectra of Eu^{2+} in $BaYF_5$: Eu^{2+},Er^{3+} containing 0.5 mole% Eu^{2+} and various concentrations of Er^{3+} at room temperature.

much smaller than the observed value. Thus the rise time is associated with a bottleneck in the multiphonon decay from the excited states in Er^{3+} after energy transfer has occurred. Using the measured values of the fluorescence decay times and the risetimes in Eq. (4), values for the nonradiative decay rate can be determined. Extrapolating this to low temperatures gives $W'(0) = 1.6 \times 10^3$ sec^{-1}. Although this represents the combined results of several different multiphonon decay processes across different size energy gaps, the dominant contribution will come from the process with the largest energy gap. For relaxation after pumping through energy transfer from Eu^{2+}, the largest gap will be between the $^2H_{9/2}$ and $^4F_{3/2}$ levels which is approximately $\Delta E = 2500$ cm^{-1}. Using this in Eq. (3) along with the values of C and α found from analyzing the temperature dependence of the fluorescence decay time gives a predicted value for $W'(0)$ of 1.4×10^3 sec^{-1}. This is almost exactly the value determined from the rise-time data and is significantly smaller than the energy-transfer rate. Thus the observed risetime is definitely associated with slow nonradiative relaxation processes and the assumptions made in analyzing the temperature dependence of the fluorescence decay time appear to be valid.

Figures 1 and 3 show that there is excellent overlap between the Eu^{2+} emission band and the $^4I_{15/2}$–$^4G_{11/2}$ absorption transitions of Er^{3+}. This can produce both radiative and radiationless energy transfer. Evidence for the radiative-transfer mechanism is provided by the reabsorption dips in the Eu^{2+} emission band corresponding to the $^4I_{15/2}$–$^4G_{4/2}$ absorption transitions of Er^{3+} as shown in Fig. 6. The area of the reabsorption dips increases with Er^{3+} concentration.

Evidence for radiationless energy transfer is provided by the change in the decay pattern of the Eu^{2+} fluorescence with increasing Er^{3+} concentration as shown in Fig. 7. The Eu^{2+} becomes nonexponential at high Er^{3+} concentrations and the lifetime becomes much shorter. The measured val-

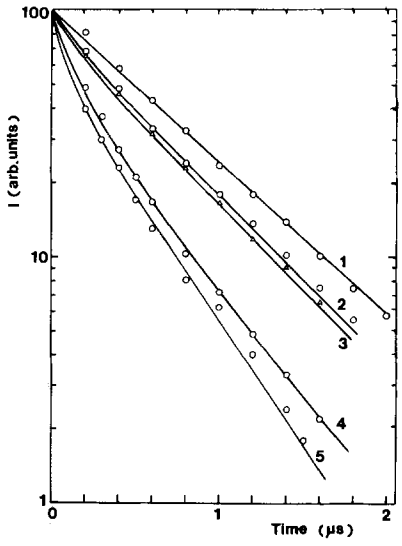

FIG. 7. Change in the Eu^{2+} decay patterns as a function of Er^{3+} concentration at room temperature in $BaYF_5$: Eu^{2+},Er^{3+} crystals containing 0.5 mole% Eu^{2+} and Er^{3+} concentrations of (1) 0.0 mole%; (2) 0.5 mole%; (3) 1.0 mole%; (4) 3.0 mole%; and (5) 5.0 mole%. (See text for explanation of theoretical lines.)

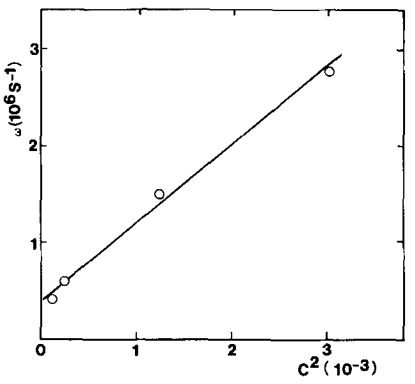

FIG. 8. Variation of Eu^{2+}–Er^{3+} energy-transfer rate with the square of the total concentration of doping ions at room temperature. The Eu^{2+} concentration was fixed at 0.5 mole% and the Er^{3+} concentrations were 0.5, 1.0, 3.0, and 5.0 mole%.

ues of the lifetimes are listed in Table I. The efficiencies (η) and rates (ω) of radiationless energy transfer were calculated from the lifetime data using the expressions

$$\omega = \tau^{-1} - \tau_0^{-1} \quad (5)$$

$$\eta = \omega/\tau^{-1} \quad (6)$$

where τ_0 is the intrinsic lifetime of the sensitizer and τ is the lifetime of the sensitizer in the presence of the acceptor. The lifetime of the sensitizer in the presence of the acceptor. The values obtained for ω and η are listed in Table I.

The mechanism for radiationless energy transfer between Eu^{2+} and Er^{3+} can be determined using the theory developed by Forster (*11*) and extended by Dexter (*12*) and Inokuti and Hirayama (*13*). In this theory the decay profile of the sensitizer after pulsed excitation is given by

$$I(t) = I(0)\exp[-t/\tau_{so} - \Gamma(1 - 3/s)(C_a/C_0)(t/\tau_{so})^{3/s}] \quad (7)$$

where τ_{so} is the intrinsic lifetime of the sensitizer emission, C_a is the activator concentration, C_0 is the critical energy-transfer concentration, and s is a number indexing the different types of electric multipole–multipole interaction. This can be used to analyze the sensitizer decay patterns in Fig. 7. The best fits to the data found using Eq. (7) are shown as solid lines. For the four double-doped samples the best theoretical fits were found using a value of $s = 6$ which implies dipole–dipole interaction. The critical energy transfer concentration was treated as an adjustible parameter and fitting the data yields an average value of $R_0 = [(4/3)\pi C_0]^{1/3} = 7.6$ Å. This critical transfer distance is related to the transfer rate by

$$\omega = \tau_{so}(R_0/R_{sa})^6 \quad (8)$$

where R_{sa} is the separation between sensitizer and activator ions. Using the values of ω listed in Table I obtained from lifetime quenching measurements and the value of R_0 obtained above, Eq. (8) gives an average sensitizer–activator separation ranging from 9.3 to 7.4 Å for these samples.

The values obtained for R_0 and ω are physically reasonable for energy transfer between a divalent and trivalent rare earth ion but it is not possible to obtain an accurate theoretical prediction for these values because a quantitative absorption spectrum cannot be obtained on the small crystallite samples presently available. An additional check on the interpretation of the energy

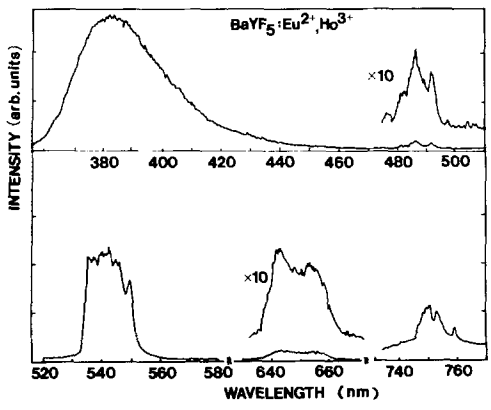

FIG. 9. Room-temperature fluorescence spectra of $BaYF_5$:Eu^{2+}(1.0 mole%),Ho^{3+}(3.0 mole%) after 337.1-nm excitation.

transfer mechanism as electric dipole–dipole interaction is obtained by plotting the transfer rate versus the square of the total concentration of doping ions as shown in Fig. 8. The fact that ω varies linearly with the square of the concentration is consistent with the square of the concentration is consistent with the predictions of dipole–dipole interaction (*14*).

Spectra of $BaYF_5:Eu^{2+},Ho^{3+}$

The room-temperature fluorescence spectra of $BaYF_5:Eu^{2+},Ho^{3+}$ after pulsed laser excitation at 337.1 nm is shown in Fig. 9. The broad band in the 380 nm spectral region is associated with the *d–f* transition of Eu^{2+}. The major emission from Ho^{3+} appears in four spectral regions: 478–497 nm ($^5F_3$–$^5I_8$); 530–560 nm ($^5S_2$–$^5I_8$); 635–663 nm ($^5F_3$–$^5I_7$ and $^5F_5$–$^5I_8$); and 746–764 nm ($^5I_4$–$^5I_8$).

The room-temperature excitation spectra of the 541 nm Ho^{3+} emission line for $BaYF_5$ samples with and without Eu^{2+} are similar to that of $BaYF_5:Eu^{2+},Er^{3+}$. The broad band associated with the *f–d* absorption transition of Eu^{2+} appears in the excitation spectrum of Ho^3 which shows the presence of energy transfer from Eu^{2+} to Ho^{3+}.

Figure 10 shows the change in the relative intensities of the Eu^{2+} and Ho^{3+} fluorescence emission as a function of Ho^{3+} concentration. The Eu^{2+} emission is quenched by the addition of Ho^{3+} due to energy transfer. The Ho^{3+} emission intensity increases up to a concentration of about 3 mole% due to increased energy transfer from the Eu^{2+}. At higher concentration levels Ho^{3+} concentration quenching occurs. The Eu^{2+} fluorescence decay time is also quenched by the addition of Ho^{3+}. The values of these lifetimes are listed in Table II.

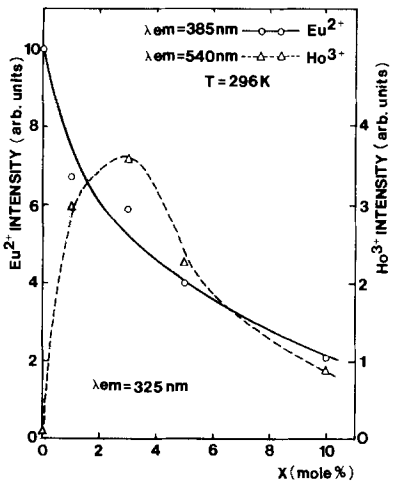

FIG. 10. Relative intensities of the Eu^{2+} (385 nm) and Ho^{3+} (541 nm) emissions at room temperature in $BaYF_5:Eu^{2+}$(1.0 mole%),Ho^{3+}(*x* mole%) as a function of *x*.

The quenching of the Eu^{2+} fluorescence intensity and lifetime by the addition of Ho^{3+} is due to the transfer of energy from the former to the latter type of ion. Using

TABLE II

Eu^{2+}–Ho^{3+} DECAY TIME AND ENERGY TRANSFER PARAMETERS (300 K)

Sample (mole %)		$\tau(\mu s)$		$t_r(\mu s)$			
Eu	Ho	Eu	Ho	Ho	η	$\omega(\mu s^{-1})$	R_0(Å)
1.0	1.0	0.34			0.32	0.94	9.8
1.0	3.0	0.30	102	13.5	0.40	1.33	5.7
1.0	5.0	0.26			0.48	1.85	5.3
1.0	10.0	0.20			0.60	3.00	5.3

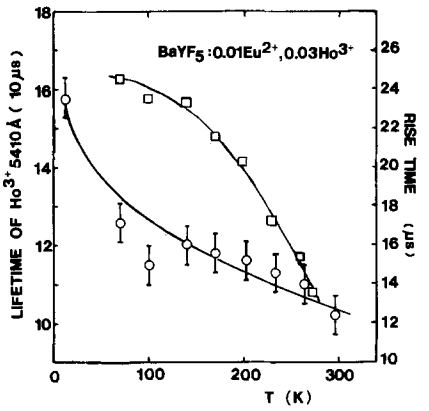

FIG. 11. Temperature dependences of the fluorescence lifetimes (circles) and rise times (squares) of Ho^{3+} in $BaYF_5$: Eu^{2+}(1.0 mole%),Ho^{3+}(3.0 mole%) after 337.1 pulsed excitation.

Eqs. (5) and (6) the transfer rate and efficiency can be determined and these are listed in Table II.

The decay profiles of the activator ions excited through energy transfer exhibit an initial rise followed by a single exponential decay. The temperature dependences of the fluorescence decay times and rise times of the Ho^3 are shown in Fig. 11 and the room-temperature values are listed in Table II. The measured rise times are again an order of magnitude larger than those predicted theoretically using Eq. (4) and the measured energy transfer rate for W_2. As before, we attribute this to a bottleneck in the radiationless relaxation processes due to weak multiphonon emission processes in this type of host crystal. However, the shape of the temperature dependence of the fluorescence lifetime can not be fit by using Eqs. (1) and (2) and thus the various parameters describing the relaxation processes cannot be determined. The different shape for the curve of the fluorescence lifetime versus temperature may be associated with the interaction between Ho^{3+} ions which occurs at the concentration present in this sample. This interaction may have an additional temperature dependence associated with it which contributes to the observed results.

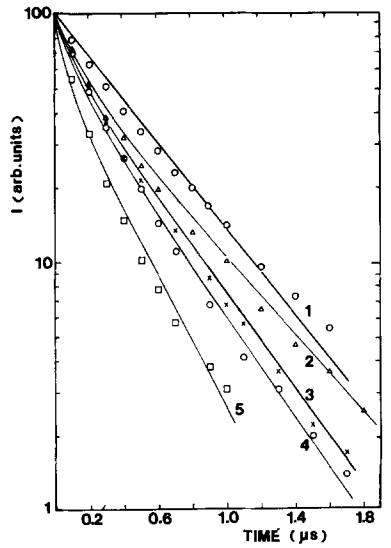

FIG. 12. Change in the Eu^{2+} decay patterns as a function of Ho^{3+} concentration at room temperature in $BaYF_5$: Eu^{2+},Ho^{3+} crystals containing 0.01 mole% Eu^{2+} and Ho^{3+} concentrations of (1) 0.0 mole%; (2) 1.0 mole%; (3) 3.0 mole%; (4) 5.0 mole%; and (5) 10.0 mole%. (See text for explanation of theoretical lines.)

The decay profiles of the sensitizer ions in the presence of activators are nonexponential due to energy transfer. These are shown in Fig. 12 for different activator concentrations. The curves are fit by the predictions of Eq. (7) assuming electric dipole–dipole interaction. The values of the critical interaction distances found from this procedure are listed in Table II. The transfer efficiency, transfer rate, and critical interaction distance for Eu^{2+}–Ho^{3+} energy transfer are smaller than the parameters found for Eu^{2+}–Er^{3+} energy transfer. This is due to the difference in spectral overlap for the two systems.

Acknowledgments

This research was supported by the U.S. Army Research Office. One of the authors (L.X.) thanks Dr. E. Banks of the Polytechnic Institute of New York for

providing experimental facilities for some of these measurements.

References

1. H. J. GUGGENHEIM AND L. F. JOHNSON, *Appl. Phys. Lett.* **15,** 51 (1969); L. F. JOHNSON AND H. J. GUGGENHEIM, *Appl. Phys. Lett.* **19,** 44 (1971); **20,** 474 (1972).
2. L. F. JOHNSON, H. J. GUGGENHEIM, J. C. RICH, AND F. W. OSTERMAGER, *J. Appl. Phys.* **43,** 1125 (1972).
3. C. FOUASSIER, B. LATOURRETTE, J. PORTIER, AND P. HAGENMULLER, *Mat. Res. Bull.* **11,** 933 (1976).
4. B. LATOURRETTE, F. GUILLEN, AND C. FOUASSIER, *Mat. Res. Bull.* **14,** 865 (1979).
5. F. GAUME, A. GROS, AND J. C. BOURCET, *Rare Earths Mod. Sci. Technol.* **3,** 143 (1982).
6. L. A. RISEBERG AND M. J. WEBER, "Progress in Optics," Vol. 14, (E. Wolf, Ed.), p. 89, North-Holland, Amsterdam, 1977.
7. L. A. RISEBERG AND H. W. MOOS, *Phys. Rev.* **174,** 429 (1968); E. D. REED, JR., AND H. W. MOOS, *Phys. Rev. B* **8,** 980 (1973).
8. M. J. WEBER, *Phys. Rev.* **171,** 283 (1968).
9. F. K. FONG, S. L. NABERHUIS, AND M. M. MILLER, *J. Chem. Phys.* **56,** 4020 (1972).
10. L. F. JOHNSON AND H. J. GUGGENHEIM, *Appl. Phys. Lett.* **23,** 96 (1973).
11. TH. FORSTER, *Ann. Phys.* **2,** 55 (1948).
12. D. L. DEXTER, *Chem. Phys.* **21,** 836 (1953).
13. M. INOKUTI AND F. HIRAYAMA, *J. Chem. Phys.* **43,** 1978 (1965).
14. F. K. FONG AND D. J. DIESTLER, *J. Chem. Phys.* **56,** 2875 (1972).